

Importance of Spin–Orbit Coupling in Hybrid Organic/Inorganic Perovskites for Photovoltaic Applications

Jacky Even,^{*,†} Laurent Pedesseau,[†] Jean-Marc Jancu,[†] and Claudine Katan^{*,‡}

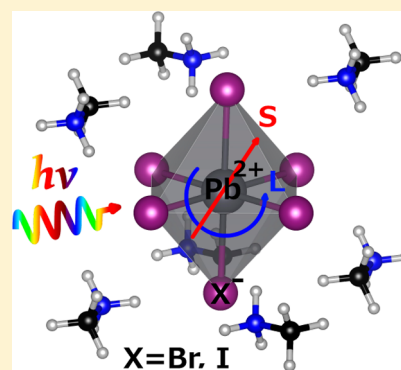
[†]Université Européenne de Bretagne, INSA, FOTON, UMR 6082, 35708 Rennes, France

[‡]CNRS, Institut des Sciences Chimiques de Rennes, UMR 6226, 35042 Rennes, France

S Supporting Information

ABSTRACT: Three-dimensional (3D) hybrid perovskites $\text{CH}_3\text{NH}_3\text{PbX}_3$ ($\text{X} = \text{Br}, \text{I}$) have recently been suggested as new key materials for dye-sensitized solar cells (DSSC) leading to a new class of hybrid semiconductor photovoltaic cells (HSPC). Thanks to density functional theory calculations, we show that the band gap of these compounds is dominated by a giant spin–orbit coupling (SOC) in the conduction-band (CB). At room temperature, direct and isotropic optical transitions are associated to a spin–orbit split-off band related to the triply degenerated CB of the cubic lattice without SOC. Due to the strong SOC, the electronic states involved in the optical absorption are only slightly perturbed by local distortions of the lattice. In addition, band offset calculations confirm that $\text{CH}_3\text{NH}_3\text{PbX}_3/\text{TiO}_2$ is a reference material for driving electrons toward the electrode in HSPC. Two-dimensional (2D) hybrids are also suggested to reach further flexibility for light conversion efficiency. Our study affords the basic concepts to reach the level of knowledge already attained for optoelectronic properties of conventional semiconductors.

SECTION: Energy Conversion and Storage; Energy and Charge Transport



Photovoltaic (PV) solar electricity is one of the key technologies of the 21st century to reduce the world's reliance on fossil fuels for energy generation. Reduced costs and higher conversion efficiencies are of crucial importance to make PV-based technologies economically more competitive. The quest for quality and performances of future solar cells has attracted a vast research effort over the past decade in the field of semiconductor heterostructures, nanostructured materials, and thin films. Various approaches ranging from high-cost/high-performance III–V technologies, multiple junctions and concentrator systems, to low-cost thin-film technologies^{1–4} have been investigated. Obviously, the design of novel and/or efficient PV devices requires a realistic modeling of underlying material's properties including chemical composition, mechanical, electrical and optical features. This can be gained with state-of-the-art *ab initio* approaches. In addition, such knowledge is desirable to reach PV cells composed of earth-abundant elements based materials.

Three-dimensional organic/inorganic perovskites, based on relatively small organic cations, have recently been suggested as a novel class of materials for dye-sensitized solar cells (DSSC) with improved photoconversion efficiency.^{5–17} Indeed, with a nanoporous TiO_2 electrode, it defines a new class of hybrid semiconductor photovoltaic cells (HSPC) with ultrahigh light power conversion efficiencies. Compared to alternative strategies based on inorganic semiconductor quantum dots (QDs) or extremely thin absorbers coated upon the internal surface of a mesoporous TiO_2 electrode, hybrid perovskites offer several benefits. In particular, the ease of synthesis,

tailoring of the optical absorption by chemical substitution, electronic transport, and high stability in dry air, are among the most featured properties of these systems. Interestingly, whereas conduction-band and valence-band alignments between absorbers and TiO_2 are of crucial importance in understanding charge transfer and charge transport,^{7,8,16,18} their modeling is still scanty.

Conversely, two-dimensional hybrid organic/inorganic materials have attracted increasing interest over the past decade due to their potential optoelectronic applications.¹⁹ Once more, the versatility of the organic part affords the possibility of fine-tuning material's properties. For example, it has been shown that the optical spectra of lead halide organic/inorganic perovskites can be easily tailored by varying the organic cation, which improves the optical efficiencies and tuning of the emission wavelength.¹⁹ Among them, self-assembled layered structures have recently shown enhanced nonlinear optical properties in microcavities.²⁰ Interestingly, in these materials density functional theory (DFT) calculations predict reversed ordering of band-edge states as compared to tetrahedrally bonded semiconductors.²¹ Consistently with important relativistic effects expected for lead, such calculations have also evidenced the major role of spin–orbit coupling (SOC) that significantly reduces the band gap by inducing a large splitting of the first degenerated conduction levels.²¹

Received: July 19, 2013

Accepted: August 20, 2013

Published: August 20, 2013

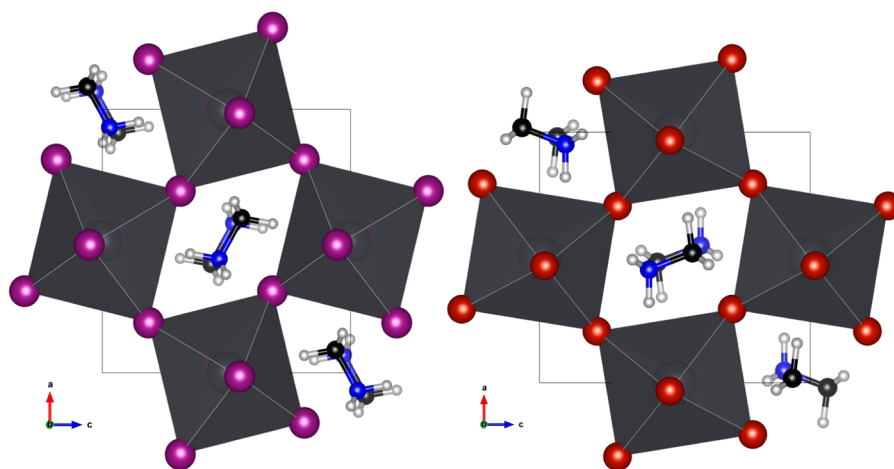


Figure 1. Overview of the crystal structures of MAPbI₃ (left) and MAPbBr₃ (right) at low temperature. The structures are both orthorhombic (space group *Pnma*),^{15,26} with a cell doubling when compared to the room temperature cubic phase.

Surprisingly, for the hybrid three-dimensional (3D) materials recently proposed as efficient HSPC,^{5,7,8,14–16} the effect of SOC has been largely overlooked, especially from the theoretical point of view. Optical absorption²² and reflectivity²³ measurements brought clear experimental evidence of sizable SOC splittings in such materials more than a decade ago. Even so, effects of SOC have been stressed in a recent computational work,¹⁵ to the best of our knowledge they have not yet been accounted for in calculated band structures reported in the literature.

This paper aims to investigate the role of SOC on the electronic band structure of two 3D hybrids recently investigated for PV-devices, namely MAPbX₃ compounds where X = Br, I and MA stands for methylammonium (CH₃NH₃). Moreover, as the design of efficient HSPC requires a good understanding of VB alignments, we suggest a protocol to derive the band alignment between the MAPbX₃ absorbers and TiO₂. It involves calculations on a slab of a related two-dimensional (2D) hybrid, namely 2(C₄H₉NH₃⁺)(PbI₄²⁻).²⁴ Such analogues also allow further comparison and offer complementary routes for band gap engineering. Actually, by mixing the composition of halogen atoms in MAPb(I_{1-x}Br_x)₃ structures, it has recently been shown that the band gap can be controllably tuned to cover the entire visible spectrum.¹⁴

These mixed compounds exhibit an averaged disordered cubic phase (space group *Pm3m*) at room temperature.²⁵ The structural disorder is both associated to the rotation of ammonium cations and tilt of lead halide octahedra. At low temperature, MAPbBr₃ and MAPbI₃ present an ordered orthorhombic structure of space-group *Pnma*, with a cell doubling when compared to the room temperature phase (Figure 1).^{15,26}

These ordered crystalline structures are used to perform the present theoretical study. Figure 2 shows the band structures of MAPbBr₃ and MAPbI₃ with and without the SOC interaction.

Let us first analyze the results obtained without SOC. Consistently with earlier results on the room temperature cubic phase,²⁷ the ground state transitions are of direct type but at the Γ -point instead of the R point.¹⁵ Our study shows that they mainly involve eight active Bloch levels: two levels for the valence-band maximum (VBM1–2) and six levels for the conduction-band minimum (CBM1–6). This apparent complex sequence at Γ -point is associated to the low temperature

symmetry breaking, which leads both to unit cell doubling and strain.²⁶ In fact, a symmetry analysis indicates that the CBM1–6 states are related to the conduction-band minimum (CBM) at the R point in the room temperature *Pm3m* cubic phase which corresponds to a triply degenerate level associated to the vectorial representation of the simple group. The same electronic band structure is obtained around the band gap for the related CsPbI₃ compound where the organic part of MAPbI₃ is replaced by a Cs atom in the low temperature *Pnma* phase (Figures S1–S2, Supporting Information). We can further develop the analysis of the electronic states using the complete phase sequence of MAPbI₃ and CsPbI₃ structures (vide infra). Similar energy dispersions occur at low temperature along the Γ –U (1/2,0,1/2), Γ –Y and Γ –U' (1/2,0,–1/2) directions in Figure 2, which is inherent to the small distortion of the perovskite lattice. The direct band gap calculated at the Γ -point is in agreement with the strong absorbance observed at room temperature.^{7,22} The six CBM1–6 states correspond to hybridizations of 6p-orbitals of lead and belong to the irreducible representations of the *D*_{2h} point group (factor group for the *Pnma* space group at Γ point). VBM1–2 consist in hybridizations of the 6s-orbitals of lead and 5p-orbitals of iodine and are associated with nonpolar irreducible representations of the point group. Optical activity is related to the dipolar matrix elements between the first valence and conduction-band states as defined by

$$M_{\text{VBM,CBM}} = \left| \left\langle \psi_{\text{VBM}} \left| -i\hbar \frac{\partial}{\partial x_i} \right| \psi_{\text{CBM}} \right\rangle \right|$$

where x_i represents the crystal axis.²¹ These matrix elements take similar values for the CBM states in the MAPbX₃ family. A strong and almost isotropic optical activity is expected from symmetry and enhanced at room temperature by the disorder of the cubic phase. We point out that a strain effect was also reported in related MASnX₃ compounds.²⁸

Figure 2 reveals large changes of the electronic band structure when accounting for SOC. Indeed, the fundamental transitions of MAPbI₃ and MAPbBr₃ lower to 0.5 eV and 0.8 eV, respectively. While the VB are nearly unaffected, the six first CB undergo a dramatic splitting. The band gap remains direct and located at the center of the Brillouin zone. These findings are consistent with the value reported for a related 2D organic–

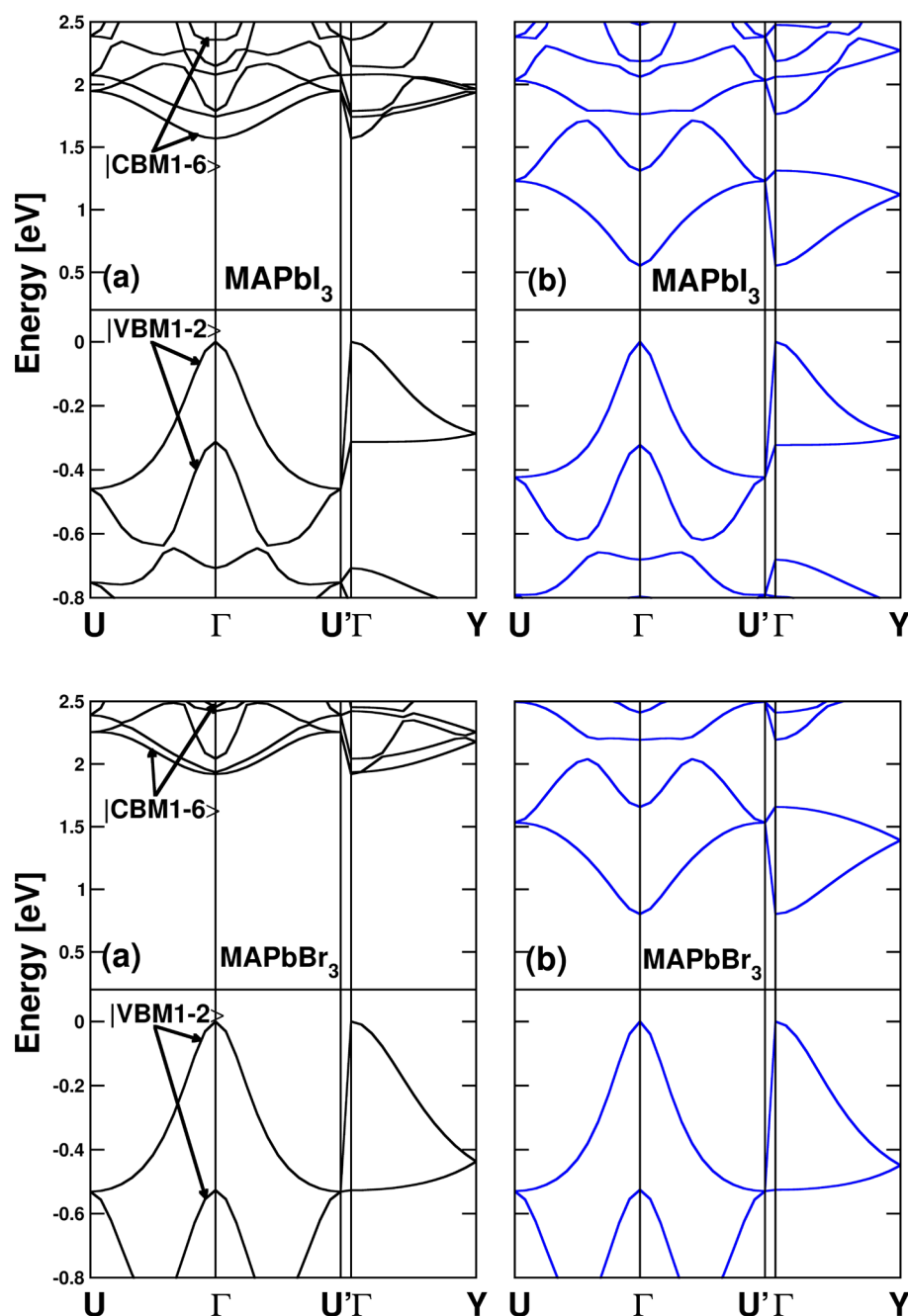


Figure 2. Electronic band structures of MAPbI₃ (top) and MAPbBr₃ (bottom), without (a) and with (b) the spin–orbit coupling interaction. The origin of the energy scale is taken at the top of the VB.

inorganic hybrid, 2(pF-C₆H₅C₂H₄-NH₃)PbI₄, for which the correction is of about 1 eV, leading to a band gap reduction by a factor of 2.²¹ This 2D perovskite crystallizes similarly to the 2(AA)PbX₄ family (AA= C_nH_{2n+1}NH₃)^{24,29,30} for which we have employed the same level of theory. For $n = 4–12$ and $X = \text{I}$, the spin–orbit coupling induces a large band gap correction of about 0.8 eV, again mainly localized on the CB levels (Figures S3–S4). Moreover, when applied to related inorganic structures such as CsPbX₃, comparable corrections are obtained, as illustrated Figure 3 (top) for the inorganic cubic phase of CsPbI₃ (a similar result is obtained for the cubic phase of CsPbBr₃²⁵ (Figures S5–S7)).

One can notice that the calculated band gap at the GGA-PBE level is equal to 1.3 eV in good agreement with previous

simulations.³¹ The calculated band-gaps at the LDA level are equal to 1.2 eV for CsPbI₃ and 1.3 eV for CsPbBr₃, and the spin–orbit coupling induces a large band gap correction of about 1.1 eV in both cases (Figure 3 (top)). All these results demonstrate that the effect of SOC on band gaps is huge and cannot be reasonably disregarded. Even if comparison with available experimental data is not straightforward, our results are in qualitative good agreement with evidence of SOC effects in the optical absorption²² and reflectivity²³ spectra reported for MAPbX₃. Furthermore, the optical transition occurs at the R point in the room-temperature *Pm3m* cubic phase. For the *Pm3m* symmorphic space group, it is possible to directly analyze the irreducible representations at R point using the *O_h* point group.³² The triply degenerate (CBM1–3) (Figure 3a

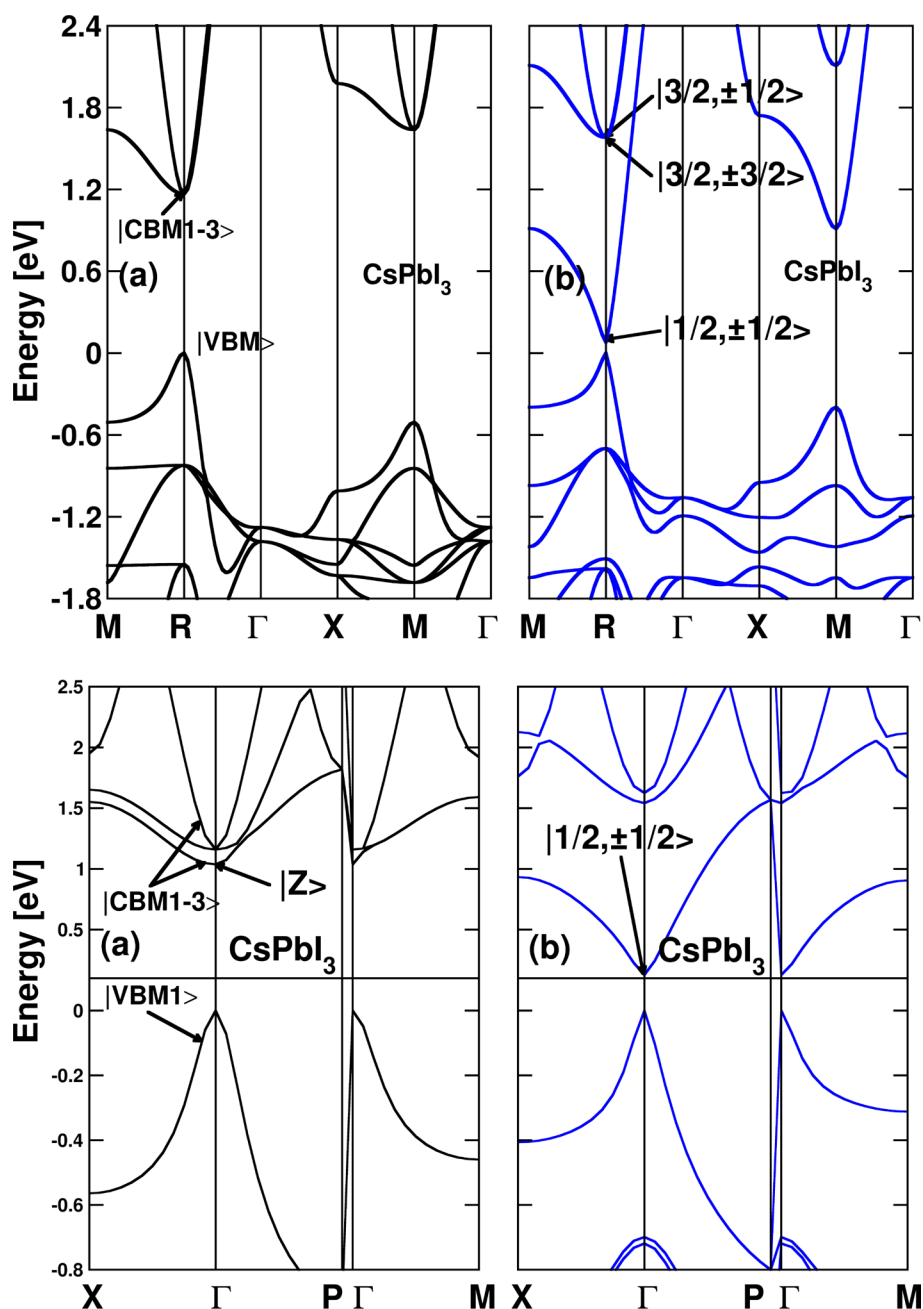


Figure 3. Electronic band structures of CsPbI₃ in the cubic phase (top) and tetragonal phase (bottom), without (a) and with (b) the spin–orbit coupling interaction. The origin of the energy scale is taken at the top of the VB.

(top)) states are associated to the vectorial representation of the simple group commonly described^{21,33} by the $|X\rangle$, $|Y\rangle$, $|Z\rangle$ symbols. In the corresponding double group including spinors, it is splitted by SOC into 2-fold degenerate states and 4-fold degenerate states (Figure 3b (top)). This situation is usually encountered in the valence band of cubic conventional semiconductors.^{21,32} The conduction band minimum of CsPbX₃ and MAPbX₃ at room temperature are associated with the 2-fold degenerate spin–orbit split-off (SO) states $|1/2, 1/2\rangle = 1/\sqrt{3}(|X + iY\rangle\uparrow) + 1/\sqrt{3}|Z\rangle\downarrow$ and $|1/2, -1/2\rangle = 1/\sqrt{3}(|X - iY\rangle\downarrow) + 1/\sqrt{3}|Z\rangle\uparrow$ (Figure 3b (top)). The SO states lead to a strong²¹ and isotropic³³ optical transition with the even $|S\rangle$ -like VBM states. To understand the influence of the cubic-tetragonal ($Pm\bar{3}m-I4mcm$) transition of MAPbI₃³⁴ on its optoelectronic properties, we have also performed DFT

calculations on CsPbI₃ in the tetragonal phase of MAPbI₃ including the SOC. Without SOC, the triply degenerate CBM states and the VBM state are folded back from the R point to the Γ point (Figure 3a, bottom). In addition and according to the D_{4h} point group, the strain along the z axis induces a small splitting of the CBM, and the band gap reduces to 1.0 eV (Figure S8). The CBM vectorial representation splits into a nondegenerate $|Z\rangle$ state (Figures S9–S10) at lower energy and 2-fold degenerate $|X\rangle$, $|Y\rangle$ states. The SOC effect is, however, much larger than the effect of strain, and leads to a very small band gap (Figure 3b (bottom)). The state ordering including SOC at the Γ point of the $I4mcm$ phase remains similar to the one of the $Pm\bar{3}m$ cubic phase, the CBM states being again related to the 2-fold degenerate SO states $|1/2, 1/2\rangle$ and $|1/2, -1/2\rangle$ (Figures S11–S12).

Based on the band structure of CsPbI_3 , we can also investigate the cubic-orthorhombic ($Pm3m-Pnma$) transition. This transition is associated to a cell doubling and folding back from the R point to the Γ point. The triply degenerate CBM are doubled and splitted by the strain along the three directions. The six CBM states correspond to one-dimensional representations of the simple D_{2h} point group, which yield 2-fold degenerate representations of the corresponding double group. The strain effect is no more negligible when compared to the SOC effect, but the CBM state of lowest energy has an electronic density similar to the one of cubic SO state.

Now, one can wonder why the fundamental transitions calculated without SOC for the low temperature $Pnma$ structures, 1.5 and 1.9 eV, respectively, for MAPbI_3 and MAPbBr_3 (Figure 2) compare nicely with the values obtained experimentally, i.e., 1.5 eV and 2.3 eV, respectively for MAPbI_3 and MAPbBr_3 .^{5,14,22,23} This agreement is fortuitous and stems from large error cancellations. Indeed, the band gap is known to be underestimated in the DFT ground-state computations. This can be corrected by including many-body effects by means of GW self-energy correction for the band gap³⁵ or using the Bethe–Salpeter equation resolution for the exciton.³⁶ Unfortunately, such calculations are beyond available computational resources for large systems. In order to gauge the importance of the GW corrections, we have considered the cubic phase of CsPbI_3 . A one-shot GW self-energy correction on the LDA level amounts to a 0.6 eV increase of the band gap. This value, although not self-consistent, shows that GW corrections are large and in the opposite direction to SOC effects. Unfortunately, a full treatment including both SOC and many-body effects is far beyond available computational resources.

Efficient electrical power generation relies on the quality of the absorber and the band gap energy. These conditions appear to be fulfilled and understood from the theoretical point of view. This efficiency also relies on the ability of the PV device to drive the carriers toward the electrodes. A correct band alignment between the sensitizer and the electrode materials is thus a key parameter to predict performances of PV devices. In the case of HSPC, with a TiO_2 electrode, hybrid MAPbX_3 perovskites appear to greatly improve the electron transport. To evaluate the valence-band alignment between the anatase structure of TiO_2 ⁸ and hybrid perovskites, a slab calculation³⁷ was performed for the $2(\text{AA})\text{PbI}_4$ with $n = 4$ (Figures S13–14). This allows estimating the offsets between the vacuum level and its bulk potential (Figure 4).

It leads to an absolute valence-band energy of -5.6 eV. Moreover, one can use the position of the 5d levels of lead as a common electronic marker both for 3D and 2D hybrid perovskites (Figures S15–S16). The relative position of the 5d-orbitals with respect to their VBM amount respectively to -16.4 and -16.2 eV. This leads to an absolute valence-band energy of -5.4 eV for both MAPbX_3 crystals that nicely agrees with the absolute valence-band energy levels deduced from the experimental work functions: -5.44 and -5.38 eV for $X = \text{I}$ and $X = \text{Br}$, respectively.⁵ The complete band alignment diagram is given Figure 5, based on the absolute valence-band energy (-7.3 eV) commonly used for TiO_2 .⁸ It is worth mentioning that similar DFT slab calculations on TiO_2 or experimental results^{38,39} yield absolute valence band energy ranging between -8.3 eV and -7.2 eV.

This clearly demonstrates that the conduction-band offsets are favorable for the electron injection from absorber to

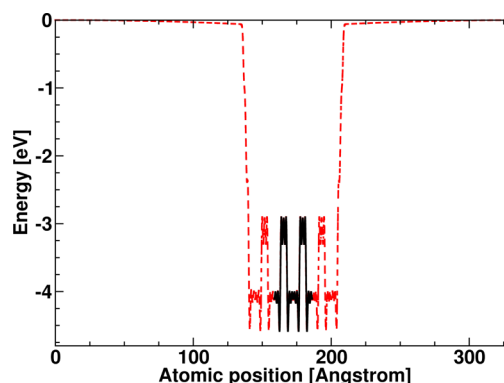


Figure 4. Potential profile in an alkyl ammonium (AA) 2D hybrid perovskite crystal (dark line) and in a slab (red dotted line) with the same crystallographic structure²⁴ surrounded by vacuum. An upward energy shift equal to 0.93 eV has been applied to the crystal profile in order to match the slab profile. When the same shift is applied to the computed VBM, an absolute VBM of -5.6 eV is found.

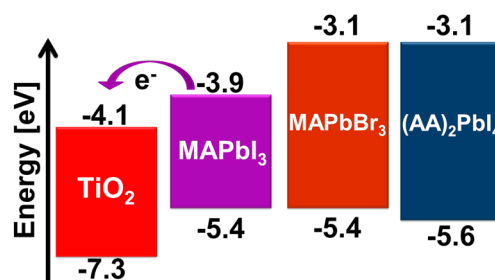


Figure 5. Energy level diagram derived from the position of Pb-5d orbitals, computed VBM (Figure 4), and experimental band gaps of MAPbI_3 (1.5 eV), MAPbBr_3 (2.3 eV),^{5,14} and an alkyl ammonium (AA) 2D hybrid perovskite (2.5 eV).²⁴ Commonly accepted values for TiO_2 electron affinity of -4.1 eV and absolute valence band energy of -7.3 eV are used.

electrode. In addition, this diagram suggests that combining 2D and 3D hybrid perovskites may provide an alternative way for the design of colorful solar cells that cover the entire visible spectrum.

In summary, based on DFT calculations, the electronic properties of 3D lead halide organic/inorganic perovskites used as absorbers in HSPC^{5,7,8} have been thoroughly investigated. Their band gap is dominated by a giant SOC effect acting mainly on the conduction band, as was already demonstrated for related 2D hybrids.²¹ At room temperature, their remarkable optical properties can be related to direct and isotropic optical transitions between a triply degenerated conduction-band and a single valence-band in a simple group representation. Valence band offsets⁵ confirm that the gathering of MAPbX_3 hybrids and TiO_2 is a relevant choice for driving the electrons toward the electrode. Our calculations on alkyl ammonium based 2D hybrids also suggest a complementary route to the chemical tuning¹⁴ recently proposed for the design of colorful solar cells with enhanced light conversion efficiency.

COMPUTATIONAL METHODS

Calculations were performed using the DFT implementation available in the ABINIT package,⁴⁰ with the LDA or the GGA-PBE gradient correction for exchange-correlation⁴¹ and relativistic, norm-conserving, separable, dual-space Gaussian-type pseudopotentials of Goedecker, Teter, and Hutter for all

atoms⁴² or Fritz-Haber-Institute's pseudopotentials.⁴³ The SIESTA code was used for the simulation of slabs at the DFT-GGA level.⁴⁴ We have verified that the band structures near the band gap do not depend on the inclusion of 5d-orbitals for Pb (Figure S8). The electronic wave functions are expanded onto a plane-wave basis set with an energy cutoff of 950 eV. $4 \times 4 \times 4$ and $4 \times 4 \times 1$ Monkhorst–Pack grids were used for reciprocal space integration in 3D and 2D structures, respectively. Calculations were performed with and without SOC.

■ ASSOCIATED CONTENT

Supporting Information

Additional computational details and structures, electronic band structures, wave function, and density plots. This material is available free of charge via the Internet at <http://pubs.acs.org>.

■ AUTHOR INFORMATION

Corresponding Authors

*E-mail: Jacky.Even@insa-rennes.fr; Tel: +33 (0)2 23 23 82 95.

*E-mail: Claudine.Katan@univ-rennes1.fr; Tel: +33 (0)2 23 23 56 82.

Notes

The authors declare no competing financial interest.

■ ACKNOWLEDGMENTS

This work was performed using HPC resources from GENCI-CINES/IDRIS grant 2013-c2012096724. The work is supported by Agence Nationale pour la Recherche (PEROCAI project ANR-10-04).

■ REFERENCES

- (1) Feltrin, A.; Freundlich, A. Material Considerations for Terawatt Level Deployment of Photovoltaics. *Renewable Energy* **2008**, *33* (2), 180–185.
- (2) Oregan, B.; Grätzel, M. A Low-Cost, High-Efficiency Solar-Cell Based on Dye-Sensitized Colloidal TiO₂ Films. *Nature* **1991**, *353* (6346), 737–740.
- (3) Grätzel, M. Solar Energy Conversion by Dye-Sensitized Photovoltaic Cells. *Inorg. Chem.* **2005**, *44* (20), 6841–6851.
- (4) Almosni, S.; Robert, C.; Thanh, T. N.; Cornet, C.; Letoublon, A.; Quinci, T.; Levallois, C.; Perrin, M.; Kuyyalil, J.; Pedesseau, L.; et al. Evaluation of InGaPn and GaAsPn Materials Lattice-Matched to Si for Multi-Junction Solar Cells. *J. Appl. Phys.* **2013**, *113* (12), 123509–123509–6.
- (5) Kojima, A.; Teshima, K.; Shirai, Y.; Miyasaka, T. Organometal Halide Perovskites as Visible-Light Sensitizers for Photovoltaic Cells. *J. Am. Chem. Soc.* **2009**, *131* (17), 6050–6051.
- (6) Im, J. H.; Lee, C. R.; Lee, J. W.; Park, S. W.; Park, N. G. 6.5% Efficient Perovskite Quantum-Dot-Sensitized Solar Cell. *Nanoscale* **2011**, *3* (10), 4088–4093.
- (7) Lee, M. M.; Teuscher, J.; Miyasaka, T.; Murakami, T. N.; Snaith, H. J. Efficient Hybrid Solar Cells Based on Meso-Superstructured Organometal Halide Perovskites. *Science* **2012**, *338* (6107), 643–647.
- (8) Etgar, L.; Gao, P.; Xue, Z. S.; Peng, Q.; Chandiran, A. K.; Liu, B.; Nazeeruddin, M. K.; Grätzel, M. Mesoscopic CH₃NH₃PbI₃/TiO₂ Heterojunction Solar Cells. *J. Am. Chem. Soc.* **2012**, *134* (42), 17396–17399.
- (9) Kim, H. S.; Lee, C. R.; Im, J. H.; Lee, K. B.; Moehl, T.; Marchioro, A.; Moon, S. J.; Humphry-Baker, R.; Yum, J. H.; Moser, J. E.; et al. Lead Iodide Perovskite Sensitized All-Solid-State Submicron Thin Film Mesoscopic Solar Cell with Efficiency Exceeding 9%. *Sci. Rep.* **2012**, *2*, 591–591–7.
- (10) Heo, J. H.; Im, S. H.; Noh, J. H.; Mandal, T. N.; Lim, C. S.; Chang, J. A.; Lee, Y. H.; Kim, H. J.; Sarkar, A.; Nazeeruddin, M. K.; et al. Efficient Inorganic–Organic Hybrid Heterojunction Solar Cells Containing Perovskite Compound and Polymeric Hole Conductors. *Nat. Photonics* **2013**, *7* (6), 487–492.
- (11) Ball, J. M.; Lee, M. M.; Hey, A.; Snaith, H. J. Low-Temperature Processed Meso-superstructured to Thin-Film Perovskite Solar Cells. *Energy Environ. Sci.* **2013**, *6* (6), 1739–1743.
- (12) Baikie, T.; Fang, Y. N.; Kadro, J. M.; Schreyer, M.; Wei, F. X.; Mhaisalkar, S. G.; Graetzel, M.; White, T. J. Synthesis and Crystal Chemistry of the Hybrid Perovskite (CH₃NH₃) PbI₃ for Solid-State Sensitized Solar Cell Applications. *J. Mater. Chem. A* **2013**, *1* (18), 5628–5641.
- (13) Qiu, J. H.; Qiu, Y. C.; Yan, K. Y.; Zhong, M.; Mu, C.; Yan, H.; Yang, S. H. All-Solid-State Hybrid Solar Cells Based on a New Organometal Halide Perovskite Sensitizer and One-Dimensional TiO₂ Nanowire Arrays. *Nanoscale* **2013**, *5* (8), 3245–3248.
- (14) Noh, J. H.; Im, S. H.; Heo, J. H.; Mandal, T. N.; Seok, S. I. Chemical Management for Colorful, Efficient, and Stable Inorganic–Organic Hybrid Nanostructured Solar Cells. *Nano Lett.* **2013**, *13* (4), 1764–1769.
- (15) Mosconi, E.; Amat, A.; Nazeeruddin, M. K.; Grätzel, M.; De Angelis, F. First Principles Modeling of Mixed Halide Organometal Perovskites for Photovoltaic Applications. *J. Phys. Chem. C* **2013**, DOI: 10.1021/jp4048659.
- (16) Park, N. G. Organometal Perovskite Light Absorbers Toward a 20% Efficiency Low-Cost Solid-State Mesoscopic Solar Cell. *J. Phys. Chem. Lett.* **2013**, *4*, 2423–2429.
- (17) Burschka, J.; Pellet, N.; Moon, S. J.; Humphry-Baker, R.; Gao, P.; Nazeeruddin, M. K.; Grätzel, M. Sequential Deposition As a Route to High-Performance Perovskite-Sensitized Solar Cells. *Nature* **2013**, *499*, 316–319.
- (18) Itzhak, Y.; Hodes, G.; Cohen, H. Band Alignment and Internal Field Mapping in Solar Cells. *J. Phys. Chem. Lett.* **2011**, *2* (22), 2872–2876.
- (19) Mitzi, D. B.; Wang, S.; Feild, C. A.; Chess, C. A.; Guloy, A. M. Conducting Layered Organic-Inorganic Halides Containing (110)-Oriented Perovskite Sheets. *Science* **1995**, *267* (5203), 1473–1476.
- (20) Wei, Y.; Lauret, J. S.; Galmiche, L.; Audebert, P.; Deleporte, E. Strong Exciton–Photon Coupling in Microcavities Containing New Fluorophenethylamine Based Perovskite Compounds. *Opt. Express* **2012**, *20* (9), 10399–10405.
- (21) Even, J.; Pedesseau, L.; Dupertuis, M. A.; Jancu, J. M.; Katan, C. Electronic Model for Self-Assembled Hybrid Organic/Perovskite Semiconductors: Reverse Band Edge Electronic States Ordering and Spin-Orbit Coupling. *Phys. Rev. B* **2012**, *86* (20), 205301–205301–4.
- (22) Tanaka, K.; Takahashi, T.; Ban, T.; Kondo, T.; Uchida, K.; Miura, N. Comparative Study on the Excitons in Lead-Halide-Based Perovskite-Type Crystals CH₃NH₃PbBr₃/CH₃NH₃PbI₃. *Solid State Commun.* **2003**, *127* (9–10), 619–623.
- (23) Hirasawa, M.; Ishihara, T.; Goto, T. Exciton Features in 0-Dimensional, 2-Dimensional, and 3-Dimensional Networks of PbI₆ 4-Octahedra. *J. Phys. Soc. Jpn.* **1994**, *63* (10), 3870–3879.
- (24) Billing, D. G.; Lemmerer, A. Synthesis, Characterization and Phase Transitions in the Inorganic–Organic Layered Perovskite-Type Hybrids (C_nH_{2n+1}NH₃)₂PbI₄, *n* = 4, 5 and 6. *Acta Crystallogr., Sect. B: Struct. Sci.* **2007**, *63*, 735–747.
- (25) Poglitsch, A.; Weber, D. Dynamic Disorder in Methyl Ammonium Trihalogenoplumbates (II) Observed by Millimeter-Wave Spectroscopy. *J. Chem. Phys.* **1987**, *87* (11), 6373–6378.
- (26) Swainson, I. P.; Hammond, R. P.; Soulliere, C.; Knop, O.; Massa, W. Phase Transitions in the Perovskite Methylammonium Lead Bromide, CH₃ND₃PbBr₃. *J. Solid State Chem.* **2003**, *176* (1), 97–104.
- (27) Umebayashi, T.; Asai, K.; Kondo, T.; Nakao, A. Electronic Structures of Lead Iodide Based Low-Dimensional Crystals. *Phys. Rev. B* **2003**, *67* (15), 155405–155405–6.
- (28) Chiarella, F.; Zappettini, A.; Licci, F.; Borriello, I.; Cantele, G.; Ninno, D.; Cassinese, A.; Vaglio, R. Combined Experimental and Theoretical Investigation of Optical, Structural, and Electronic Properties of CH₃NH₃SnX₃ Thin Films (X = Cl, Br). *Phys. Rev. B* **2008**, *77* (4), 045129–045129–6.

- (29) Billing, D. G.; Lemmerer, A. Synthesis, Characterization and Phase Transitions of the Inorganic–Organic Layered Perovskite-Type Hybrids $(C_nH_{2n+1}NH_3)_2PbI_4$ ($n = 12, 14, 16$ and 18). *New J. Chem.* **2008**, 32 (10), 1736–1746.
- (30) Lemmerer, A.; Billing, D. G. Synthesis, Characterization and Phase Transitions of the Inorganic–Organic Layered Perovskite-Type Hybrids $(C_nH_{2n+1}NH_3)_2PbI_4$, $n = 7, 8, 9$ and 10 . *Dalton Trans.* **2012**, 41 (4), 1146–1157.
- (31) Murtaza, G.; Ahmad, I. First Principle Study of the Structural and Optoelectronic Properties of Cubic Perovskites $CsPbM_3$ ($M = Cl, Br, I$). *Physica B* **2011**, 406 (17), 3222–3229.
- (32) Bir, G. L.; Pikus, G. E. *Symmetry and Strain-Induced Effects in Semiconductors*; Wiley: New York/Toronto, 1974.
- (33) Chuang, S. *Physics of Optoelectronic Devices*; Goodman, J. W. Ed.; Wiley: New York, 1995.
- (34) Kawamura, Y.; Mashiyama, H.; Hasebe, K. Structural Study on Cubic-Tetragonal Transition of $CH_3NH_3PbI_3$. *J. Phys. Soc. Jpn.* **2002**, 71, 1694–1697.
- (35) Hedin, L. New Method for Calculating 1-Particle Greens Function with Application to Electron-Gas Problem. *Phys. Rev.* **1965**, 139 (3A), A796–A823.
- (36) Salpeter, E. E.; Bethe, H. A. A Relativistic Equation for Bound-State Problems. *Phys. Rev.* **1951**, 84 (6), 1232–1242.
- (37) Prodhomme, P. Y.; Fontaine-Vive, F.; Van der Geest, A.; Blaise, P.; Even, J. Ab Initio Calculation of Effective Work Functions for a $TiN/HfO_2/SiO_2/Si$ Transistor Stack. *Appl. Phys. Lett.* **2011**, 99 (2), 022101–022101–3.
- (38) Kang, W.; Hybertsen, M. S. Quasiparticle and Optical Properties of Rutile and Anatase TiO_2 . *Phys. Rev. B* **2008**, 82 (8), 085203–085203–11.
- (39) Scanlon, D. O.; Dunnill, C. W.; Buckeridge, J.; Shevlin, S. A.; Logsdail, A. J.; Woodley, S. M.; Catlow, C. R. A.; Powell, M. J.; Palgrave, R. G.; Parkin, I. P.; et al. Band Alignment of Rutile and Anatase TiO_2 . *Nat. Mater.* **2013**, DOI: 10.1038/NMAT3697.
- (40) Gonze, X.; Amadon, B.; Anglade, P. M.; Beuken, J. M.; Bottin, F.; Boulanger, P.; Bruneval, F.; Caliste, D.; Caracas, R.; Cote, M.; et al. ABINIT: First-Principles Approach to Material and Nanosystem Properties. *Comput. Phys. Commun.* **2009**, 180 (12), 2582–2615.
- (41) Perdew, J. P.; Burke, K.; Ernzerhof, M. Generalized Gradient Approximation Made Simple. *Phys. Rev. Lett.* **1996**, 77 (18), 3865–3868.
- (42) Hartwigsen, C.; Goedecker, S.; Hutter, J. Relativistic Separable Dual-Space Gaussian Pseudopotentials from H to Rn. *Phys. Rev. B* **1998**, 58 (7), 3641–3662.
- (43) Fuchs, M.; Scheffler, M. Ab Initio Pseudopotentials for Electronic Structure Calculations of Poly-Atomic Systems Using Density-Functional Theory. *Comput. Phys. Commun.* **1999**, 119 (1), 67–98.
- (44) Soler, J. M.; Artacho, E.; Gale, J. D.; Garcia, A.; Junquera, J.; Ordejon, P.; Sanchez-Portal, D. The SIESTA Method for Ab Initio Order-N Materials Simulation. *J. Phys.: Condens. Matter* **2002**, 14 (11), 2745–2779.